Development of methods for analysis and reconstruction of nuclear medicine images

Implementation of the medical Physics, Oncology & Nuclear medicine research image platform at Sahlgrenska Academy

Tobias Rydén

Department of radiation physics

Institute of clinical sciences

Sahlgrenska Academy at University of Gothenburg

UNIVERSITY OF GOTHENBURG

Gothenburg 2016

Cover illustration: PhONSAi showing SPECT images reconstructed with ST-OSEM and SARec-OSEM. © Jens Hemmingsson

Till Peter Lundblad (1945-2005)

Development of methods for analysis and reconstruction of nuclear medicine images

Implementation of the medical Physics, Oncology & Nuclear medicine research image platform at Sahlgrenska Academy

Tobias Rydén

Department of radiation physics, Institute of clinical sciences
Sahlgrenska Academy at University of Gothenburg
Göteborg, Sweden

ABSTRACT

This thesis presents four novel algorithms for processing and analysis of nuclear medicine images. In addition, the novel research image platform where these four algorithms have been implemented, together with most established algorithms for image processing and analysis, are shortly described. The majority of the algorithms in the image platform are executed on the graphics processing unit (GPU), which enable fast parallel execution of the scripts.

The four novel algorithms have been constructed for analysis of nuclear medicine images of patients with neuroendocrine tumours, who has either been diagnosed or treated with the somatostatin analogues ^{111}In-octreotide and ^{177}Lu-octreotate, respectively. The first algorithm was constructed for analysis of two planar image methods for kidney dosimetry. The results of the analysis showed that it is most challenging to find a region of interest (ROI) that resembles the true activity in the over- and underlying tissue of the kidney. Nevertheless, in this paper we propose that a ROI surrounding the kidney might be preferable over small ROIs. Furthermore, due to the high influence of background activity in the anterior image it seems to be favourable to perform the dosimetry on the posterior image instead of using the geometric mean value of the anterior and posterior images. The second algorithm was constructed for obtaining good estimates of the bone marrow doses from planar images. The algorithm generated estimates of the absorbed dose to bone marrow that were in agreement with earlier estimates. In addition, the obtained absorbed doses correlated to haematological response. The third algorithm was constructed for improved diagnosis of liver tumours. The methodology was based on a statistical approach for separating livers with tumour involvement from livers without tumour involvement. The method showed promising

results in a retrospective study where an increased number of patients with liver tumour involvement could be diagnosed. Finally, a new Monte Carlo-based single photon emission computed tomography reconstruction algorithm was constructed. Since the code is executed on the GPU the tremendous number of photon emission and scattering is rapidly simulated in parallel. Thereby, the simulation time for the reconstruction is only a few minutes. In phantom measurement this reconstruction method was superior to the conventional and the state-of-the-art methods used for reconstruction of clinical images.

SAMMANFATTNING PÅ SVENSKA

Denna avhandling presenterar fyra nya algoritmer för bearbetning och analys av nuklearmedicinska bilder. I avhandlingen presenteras också den nya bildplattform som är framtagen för att effektivt använda dessa algoritmer tillsammans med andra etablerade algoritmer för bildbehandling. Majoriteten av algoritmerna i bildplattformen har skrivits för att kunna köras på grafikkort. Detta möjliggör parallell körning, vilket innebär att algoritmerna blir väldigt snabba.

De fyra nya algoritmerna har konstruerats för analys av nuklearmedicinska bilder av patienter med neuroendokrina tumörer, som antingen har diagnostiserats eller behandlats med de radionuklidmärkta somatostatinanalogerna ^{111}In-oktreotid och ^{177}Lu-octreotat.

Den första algoritmen konstruerades för analys av två bildbaserade metoder för njurdosimetri. Resultaten av analysen visade att det är svårt att hitta ett bakgrundsområde som motsvarar den verkliga aktiviteten i över och underliggande vävnad hos njuren. Det som bäst motsvarar detta är området runt hela njuren och inte ett enskilt mindre område bredvid njuren som används vid kliniska studier. Dessutom tycks den höga signalpåverkan från bakgrundsaktiviteten i den främre bilden göra att det är fördelaktigt att utföra dosimetri på den bakre bilden istället för att använda det geometriska medelvärdet av den främre och bakre bilden.

Den andra algoritmen konstruerades för att, från planara bilder, erhålla bra uppskattning av benmärgsdosen. Algoritmen genererade absorberade benmärgsdoser som överensstämde med tidigare uppskattade benmärgsdoser. Dessutom korrelerade de erhållna benmärgsdoserna till hematologisk respons, vilket sällan har rapporterats.

Den tredje algoritmen konstruerades för att erhålla förbättrad diagnos av levertumörer. Metodiken i arbetet bygger på ett statistiskt tillvägagssätt för att separera levrar med tumörer från levrar utan tumörer. Resultaten visade lovande resultat i en retrospektiv studie, där ett ökat antal patienter med levertumörer kunde detekteras.

Slutligen konstruerades en ny Monte Carlo-baserad rekonstruktionsalgoritm för att förbättra rekonstruktionen av tredimensionella bilder. Eftersom koden kördes på grafikkort kunde simulering av miljardtals fotoner snabbt beräknas. Därigenom blev simuleringstiden för rekonstruktionen av tredimensionella bilder endast några minuter. Rekonstruktionsmetoden testades genom

fantommätningar där den visade sig vara betydligt bättre än konventionella metoder, samt bättre än de allra senaste kommersiella rekonstruktionsmetoderna med integrerad upplösningskorrektion.

LIST OF PAPERS

This thesis is based on the following studies, referred to in the text by their Roman numerals.

I. **Magnander* T**, Svensson J, Båth M, Gjertsson P, Bernhardt P. Improved planar kidney activity concentration estimate by the posterior view method in ^{177}Lu-DOTATATE treatments. Radiat. Prot. Dosimetry 2016;169(1-4):259-266. (Open access)

II. Svensson J, **Rydén T**, Hagmarker L, Hemmingsson J, Wängberg B, Bernhardt P. A novel planar image based method for bone marrow dosimetry in ^{177}Lu-DOTATATE treatments correlates with haematological toxicity. EJNMMI Physics, 3(1), 1-12. (Open access)

III. **Magnander* T**, Wikberg E, Svensson J, Gjertsson P, Wängberg B, Båth M, Bernhardt P. A novel statistical analysis method to improve the detection of hepatic foci of ^{111}In-octreotide in SPECT/CT imaging. EJNMMI Phys. 2016;3(1):1. (Open access)

IV. **Rydén T**, Heydorn-Lagerlöf J, Hemmingsson J, Svensson J, Båth M, Gjertsson P, Bernhardt P. Fast GPU based Monte Carlo code for SPECT/CT reconstructions generates improved quality of ^{177}Lu images. Manuscript.

*Magnander was the author's name until 2016

OTHER RELATED PUBLICATIONS

1. Cederkrantz E, Andersson H, Bernhardt P, Bäck T, Hultborn R, Jacobsson L, Jensen H, Lindegren S, Ljungberg M, **Magnander* T**, Palm S, Albertsson P. Absorbed Doses and Risk Estimates of ^{211}At-MX35 F(ab')2 in Intraperitoneal Therapy of Ovarian Cancer Patients. Int J Radiat Oncol Biol Phys. 2015 Nov 1;93(3):569-76

2. Svensson J, Hagmarker L, **Magnander* T**, Wängberg B, Bernhardt P. Radiation exposure of the spleen during ^{177}Lu-DOTATATE treatment and its correlation with haematological toxicity and spleen volume. EJNMMI Phys. 2016 Dec;3(1):15.

*Magnander was the author's name until 2016

CONTENT

ABBREVIATIONS

AP   Anterior-Posterior

ARF   Angular Response Function

BTR   Background to True background Ratio

CCL   Connected Component Labelling

ConjV   Conjugate View

CPU   Central Processing Unit

CT   Computed Tomography

CUDA   Compute Unified Device Architecture

CV   Coefficient of Variation

DICOM   Digital Imaging and Communications in Medicine

FBP   Filtered Back Projection

FOV   Field Of View

FWHM   Full Width at Half Maximum

GPGPU   General-Purpose computing on Graphics Processing Units

GPU   Graphics Processing Unit

HB   Haemoglobin

HU   Hounsfield Unit

LEHR	Low Energy High Resolution
MC	Monte Carlo
MEGP	Medium Energy General Purpose
MLEM	Maximum Likelihood Expectation Maximization
NET	Neuroendocrine Tumour
nNUF	normalised Number of Uptake Foci
nNUFTI	normalised Number of Uptake Foci vs Threshold Index
nThI	normalised Threshold Index
OSEM	Ordered Subset Expectation Maximization
PA	Posterior-Anterior
PET	Positron Emission Tomography
PhONSA	The medical Physics, Oncology & Nuclear medicine research group at Sahlgrenska Academy
PhONSAi	The medical Physics, Oncology & Nuclear medicine research image platform at Sahlgrenska Academy
PLT	Platelet counts
PM	Photo Multiplier
PostV	Posterior View
radtech	Radiological techniques

RAM	Random Access Memory
ROI	Region Of Interest
RRC-OSEM	OSEM with resolution recovery and attenuation correction
SARec	The Sahlgrenska Academy Reconstruction code (the Monte Carlo code in PhONSAi)
SARec-OSEM	The Monte Carlo-based OSEM algorithm in PhONSAi
SDK	Software Development Kit
SPECT	Single Photon Emission Computed Tomography
ST-OSEM	Standard OSEM with CT-based attenuation correction
ThI	Threshold Index
TNC	Tumour to Normal tissue Concentration ratio
VOI	Volume Of Interest
VTK	Visualization Toolkit
WBC	White Blood Cells

1 INTRODUCTION

This project was performed within nuclear medicine physics and had the main goal to develop new methods for analysis of kidney and bone marrow dosimetry and diagnostics of tumour involvement in the liver, as well as to create a novel Monte Carlo-based reconstruction method for single photon emission computed tomography (SPECT). For optimal performance in such analysis and in quantification in medical images, different algorithms for image processing, segmentation and reconstruction are required. Furthermore, in many situations several different algorithms may be needed for one specific goal. However, in commercial medical image platforms the flexibility is restricted to the implemented algorithms, and even if some possibility of creating new algorithms exists, e.g. in workstations such as Xeleris (GE Healthcare, USA), it is cumbersome to integrate them with existing algorithms and to achieve time-effective methods. Therefore, one additional purpose of this project was to develop a flexible and robust imaging platform to use in medical image research: the medical Physics, Oncology and Nuclear medicine research image platform at Sahlgrenska Academy (PhONSAi).

1.1 Gamma camera images

A gamma camera is a device used to image photon-emitting radionuclides in patients. The basic components in a camera are the collimator, the crystal, the photo multiplier (PM) tubes and the associated electronics for collecting and analysing the signal from the PM tubes. The most common crystal material is NaI(Tl) and the collimator is usually made of lead. When an incoming photon interacts with the crystal, visible light is emitted and converted to an electrical signal in the PM tubes. The difference in the signal in the different PM tubes are used to obtain the spatial information. The total signal is proportional to the incoming photon energy (energy departed in the crystal).

To obtain information of where in the patient the detected photon may have originated from, a collimator is used. The most used collimator is the parallel hole collimator with hexagonal holes, which discriminates almost all of the photons that are not directed perpendicular to the detector. The maximum angle of incidence through the collimator is determined by the hole diameter and hole length. The camera system sensitivity depends on the collimator design. Many deep holes with small diameter provide a high resolution but poor sensitivity, since the maximum angle is small in such a case. With larger hole diameters the maximum angle will increase and more photons will contribute to the image, resulting in a higher sensitivity and lower noise at the

cost of resolution. The sensitivity and resolution also depend on the thickness of the crystal. A thicker crystal provides increased sensitivity but lower resolution. If the collimator walls, septa, are too thin, or if the photon energy is too high, photons may penetrate the septa, giving star artefacts in the image and reducing the resolution.

A gamma camera is able, with some uncertainty, to determine the incoming photon energy. The full width at half maximum (FWHM) for the energy resolution is usually around 10%. Most radionuclides that are imaged with the gamma camera are emitting photons with discrete energies. It is therefore possible to discriminate scattered photons by using an energy window around the photo peak of the source. The energy windows are a software setting that decides which detected pulses should be registered and contribute to the image. Because of the somewhat poor energy resolution and the low sensitivity, it is mandatory to collect photons within quite a broad energy window around the energy peak. Therefore, scattered photons will also be included in the image, which will decrease the contrast in the image. The low sensitivity of the camera and the limited acquisition times in clinical practice will result in noisy images. Further image degrading effects are due to variable attenuation and resolution for different source locations in the patient. Photons emitted from a volume of the patient that is behind bone or other high attenuating materials contribute less to the resulting image than photons emitted from a volume with lower attenuation tissues (e.g. lungs) between the volume and the camera. Since the maximum angle is fixed for a parallel hole collimator, a point source far away from the camera will be more blurred than a point source that is close to the camera. However, the sensitivity for the point sources will be the same. Due to the increased blurring, or partial volume effect, with distance, it is beneficial to have the camera as close to the patient as possible. Due to the described image degrading effects the resulting gamma camera image is not a perfect projection of the activity concentration in the patient. It is an attenuated, blurred and noisy projection with scattered photons included.

1.2   SPECT reconstructions

In SPECT, gamma camera images, projections, are acquired around the patient. The three-dimensional activity concentration distribution in the patient is then reconstructed with a reconstruction algorithm. For an infinite number of perfect projections around the patient, the collected data would have been the Radon transform of the activity concentration distribution. The Radon transform has an inverse. The inverse Radon transform is usually called filtered back projection (FBP). FBP has been used for a long time, mainly because it is very fast and not so computing intensive. One disadvantage of FBP on noisy

SPECT raw data is that the noise will be amplified. This can be handled by some modification of the filter in the FBP or by using post filters. There are methods to correct for scattering and attenuation in FBP-reconstructed images, but they are not optimized for non-uniform attenuation.

A more optimal way to reconstruct SPECT is to use iterative reconstructions. The basic principle in iterative reconstructions is to guess a tomographic solution (estimate) and project it (a forward projection) for the same angles as the projections have been measured around the patient. Often 60 to 120 angles are used. The forward projections are then compared with the measured projections. The difference between the projections is used for updating the estimated image (back projection). This procedure is repeated until the difference is minimized or stopped at a predefined number of iterations. The most common iterative method in SPECT reconstruction is based on maximum likelihood expectation maximization (MLEM). It is a statistical method that assumes Poisson distributed detected pulses [1]. In MLEM the following calculation is performed for every voxel in the estimate (f_j):

$$\bar{f}_j^{(k+1)} = \frac{\bar{f}_j^k}{\sum_{i=1}^n a_{ij}} \sum_{i=1}^n \frac{g_i}{\sum_{j=1}^m a_{ij} \bar{f}_j^{(k)}} a_{ij},$$

<div align="right">Eq. 1</div>

where a_{ij} is the probability that the emitted photon from f_j will be detected in bin i. $\sum_{i=1}^n \frac{g_i}{\sum_{j=1}^m a_{ij} \bar{f}_j^{(k)}}$ is the quote of the measured (g_i) and the current estimated counts in bin i and $\sum_{i=1}^n \frac{g_i}{\sum_{j=1}^m a_{ij} \bar{f}_j^{(k)}} a_{ij}$ is the back projection of that quote.

Since these calculations are done for the whole estimate, matrix sizes of 128^3-512^3 (2-134 millions) voxels, it is very computing intensive and time consuming for a central processing unit (CPU). However, all these steps can be done in parallel and have therefore been included as a graphics processing unit (GPU) code in PhONSAi. This speeds up the reconstruction time by a factor of up to 1000 compared to a CPU-based algorithm.

MLEM converges rather slowly (40-100 iterations). To speed up the convergence the projections can be divided into subsets. An example of how to order 120 projections in subsets follows:

Subset 1: 1, 11, 21, 31, 41, 51, 61, 71, 81, 91, 101, 111

Subset 2: 2, 12,…   112

<div align="center">…</div>

Subset 10: 10, 20,…   120

The method is called ordered subset expectation maximization or OSEM. It is comparable to MLEM as the number of subsets are moderate, but converges the number of subsets times faster [2]. With the MLEM and OSEM algorithms, all image degrading effects could theoretically be included and corrected for so that the algorithm will converge to the most probable activity concentration distribution. The commercial iterative reconstruction algorithms have had CT-based attenuation correction included for a long time in MLEM and OSEM (ST-OSEM), i.e. the calculated projections are attenuated by the CT in the same way as the measured projections are presumed to have been by the patient. A correction for the depth dependent collimator response (RRC-OSEM) has been included in the commercial algorithms recently.

The disadvantages of the iterative algorithms have been that they require much more computations. With today's technology this is no longer a major problem. The advantage is that it is possible to model the physics so that the validity of the reconstruction increases. All reconstruction algorithms in PhONSAi are written in Compute Unified Device Architecture, CUDA, and use the GPU, making it possible to use full Monte Carlo simulations of the forward projections in the Sahlgrenska Academy reconstruction code (SARec), which is presented in Paper IV.

1.3 Nuclear medicine diagnosis and therapy of neuroendocrine tumours

The subjects involved in this study are patients that have undergone nuclear medicine diagnostics and therapy of neuroendocrine tumours (NETs). These tumours originate from neuroendocrine cells, which are cells that act like an interface between the nervous system and the endocrine system [3]. Some NETs overexpress somatostatin receptors and could therefore be targeted with radiolabelled somatostatin analogues such as ^{111}In-octreotide for diagnostics and ^{177}Lu-DOTA-octreotate for therapy [4].

1.4 The isotopes used in this thesis

1.4.1 ^{111}In for gamma camera imaging

The radionuclide ^{111}In, which is labelled to octreotide by the chelat DTPA, is used for diagnosis of NETs by planar scintigraphy and SPECT. [111]In has two gamma emissions that can be used for gamma camera imaging. One has an

energy of 171.3 keV with a branching ratio of 90% and the other has an energy of 245.4 keV with a branching ratio of 94% [5]. The half-life of ^{111}In is 2.8 days. In ^{111}In imaging with gamma cameras both gamma emissions can be used, and dual energy window settings are often used over the 171.3 and 245.4 keV photo peaks. The use of both photo peaks increases the signal in the image and thereby the noise will be reduced. This is of beneficial value for the image quality. However, photons from the 245.4 keV emissions will be scattered into the 171.3 keV window, which will decrease contrast and resolution. Different methods for reducing the scattering in gamma camera images have been proposed and the triple energy window (TEW) method is one method that can be used in clinical applications [6]. However, TEW will increase the noise in the image and is therefore not always of beneficial value.

1.4.2 ^{177}Lu for gamma camera imaging and dosimetry

[177]Lu is a beta emitter with a half-life of 6.7 days and a maximum beta energy of 498.3 keV, which can be considered as a medium energy suitable for therapy of disseminated tumour disease [7]. Labelled to the somatostatin analogues octreotate, by the chelat DOTA, it is today used worldwide for therapy of neuroendocrine tumours. [177]Lu also emits a low abundance of photons, where the 208 and 113 keV gamma photons with branching ratios of 11 and 6.4 %, respectively, can be used for gamma camera imaging. However, due to the high in-scattering from the 208 keV gamma photons into the 113 keV energy window, a single energy window over 208 keV is preferable [8]. The ability to achieve rather good image quality with ^{177}Lu enables the possibility to quantify the activity uptake and perform post-dosimetric calculations. This is most valuable for estimating the number of treatments that can be given to the patients. Today, most treatment protocols with ^{177}Lu-DOTATATE are based on the patient's status, regarding e.g. blood values and kidney function, and the accumulated mean absorbed dose to the kidneys. The dose limits to the kidneys are often restricted to 24-27 Gy [9]. However, kidney toxicity is seldom observed at these dose levels and in the ILUMINET study, which is performed at Sahlgrenska University Hospital and Skåne University Hospital, the maximum biological effective dose is set to 40 Gy for patients with good kidney function. The notable radiation toxicity in the patients is bone marrow response. Often this response is transient, but in some cases it might be irreversible [10]. Therefore, an estimate of the bone marrow dose would be beneficial in the treatment planning. However, it is most challenging to quantify the low bone marrow uptake in both planar images and SPECT. Only one study has in a selected patient group reported a correlation between the bone marrow response and absorbed dose [11]. For obtaining further improved

absorbed dose and response correlations, new methods for the bone marrow dosimetry would by valuable.

1.5 The conjugate view method for planar imaging dosimetry

The conjugate view (ConjV) method is commonly used in 2D dosimetry for estimation of the activity concentration in organs and tumours [12]. An advantage of the ConjV method is that it is independent of the depth of the source, i.e. the organ or tumour of interest. Most gamma cameras have two opposite detectors that simultaneously acquire photons emitted from the patient, thereby one anterior-to-posterior (AP) and one posterior-to-anterior (PA) image are obtained during a single scan. Whole body scanning is often performed within 15 to 30 minutes.

By using the geometric mean between these two projections, the source depth dependence is eliminated [13]. The geometric mean of two opposite projections is the square root of the product of the projections. The parameters for activity estimation with the conjugate view method are the effective attenuation coefficient μ_e, the sensitivity of the camera system k, the patient thickness T and the thickness of the organ to be measured t. The activity is:

$$A = \frac{\sqrt{C_A C_P} \cdot e^{\frac{\mu_e T}{2}} \cdot \mu_e t}{k(1 - e^{-\mu t}) \cdot e^{\frac{\mu_e t}{2}}}$$

Eq. 2

where C_A is the number of net counts in the AP projection and C_P is the number of net counts in the mirrored PA projection. The effective attenuation coefficient μ_e and the calibration factor k are measured with a source of known activity at known depths in tissue-equivalent material. The calibration source should have similar size as the source of interest for obtaining the best estimate of the scattering contribution (the build-up factor) in this broad beam geometry. When the activity uptake in the source of interest is well above a homogenous background in both the AP and PA projections, the conjugate view method is a rather robust and straightforward method with good precision. However, if the source of interest is close to any AP or PA surface, the signal in the opposite projection might be close to the background signal. Furthermore, in reality the background activity is heterogeneously distributed and it is not obvious how a background region of interest (ROI) should be positioned for resembling the true over- and underlying tissue contribution in the source ROI.

1.6 Renal dosimetry

In ^{177}Lu treatments with somatostatin analogues, a maximal mean absorbed renal dose of 24-27 Gy is used [14, 15]. Determination of the estimated renal dose is often done in 2D images with the conjugate view method [12]. However, overlapping organs and tumours in the planar image is a major problem in the activity estimation with the ConjV method. If a background correction is performed, a ROI is placed somewhere around the kidney, which, when rescaled, is supposed to resemble the activity ahead of and behind the kidney (Figure 1). However, no consensus on the location of the background ROI exists and it would be valuable to investigate how different background locations influence the estimated absorbed doses. Furthermore, due to the posterior location of the kidney the ConjV method might not be the superior method, and an alternative is to only use the posterior gamma camera image [16].
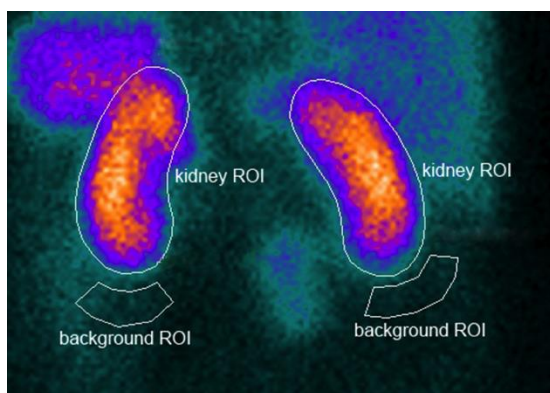

Figure 1. 2D ROIs over the kidneys and the background.

1.7 Bone marrow dosimetry

In contrast to renal toxicity, which seldom is observed in ^{177}Lu-DOTATATE treatments, bone marrow responses are almost always observed [17, 18]. Most often the bone marrow response is mild and transient, but in some cases it might be manifested and life threatening which limit further treatments. To perform accurate bone marrow dose estimations in planar images is most challenging, due to the low activity concentration in the bone marrow and high activity concentration in overlapping organs. Even in SPECT images the low activity concentration in the bone marrow is challenging to determine accurately. The factors that make it problematic are noise, scattering and the

pronounced partial volume effect for the small bone marrow cavities. Therefore, an indirect estimation of blood-based dosimetry is often performed, which assumes a constant ratio between the activity concentration in blood and bone marrow [19]. Only in one selected study with limited number of patients a dose response correlation has been observed [11]. It is therefore appealing, and most challenging, to find new methodology for obtaining bone marrow doses from planar imaging that also correlate with haematological response.

1.8   Detection of liver tumours

It can sometimes be difficult to determine whether an uptake focus in the liver is normal or a sign of malignancy. This is often the case when the tumours are small (around a few grams) or the uptake of the radiopharmaceutical is low. The standard method used for review of the SPECT images is a subjective visual assessment. However, since SPECT images of the liver are noisy and the resolution is low, it is most challenging to correctly diagnose small tumours, with low uptake to normal tissue ratio, by visual inspection [20]. Therefore, it might be valuable to find alternative, automatic, methods to analyse the noise distribution in healthy and malignant tissues and investigate if any difference between them exists. Furthermore, most importantly, judge if this difference can be used as a basis for an automatic analysis method of tumour involvement in the liver. One way to characterize the noise in the liver in an objective way might be to study the number of segmented uptake foci for different thresholds, where the counting could be performed with a connected-component labelling (CCL) algorithm, which is one of all algorithms that have been included in PhONSAi.

1.9   Monte Carlo based SPECT/CT reconstructions

When the activity distribution in a patient is captured by a gamma camera, through the emitted photons, it is not a perfect ray projection. The image has been degraded by attenuation and scattering in the patient and blurred by the collimator and the crystal, as described in 1.1. In OSEM a perfect ray projection or an attenuated perfect ray projection is often used in the forward projection, with the result that the algorithm converges to a slightly erroneous activity concentration distribution. In commercial algorithms, attenuation correction is implemented and, in state-of-the-art algorithms, the collimator response is also implemented in the forward projections. This results in improved image quality but still these algorithms are approximated solutions of the problems. Recently, some research groups have presented MC-based

OSEM SPECT/CT reconstructions, which have the potential to correctly include degrading effects like scattering, partial volume effects and attenuation [21]. The procedure is shown in Figure 2. However, this is very computationally intensive for the used CPU- and MC-based reconstructions, and the simulation time often is days. This is beyond clinically useful reconstruction times. Nevertheless, implementation of the MC reconstruction with CUDA programming will enable parallelisation of the code and thereby decreased simulation times could be obtained [22].
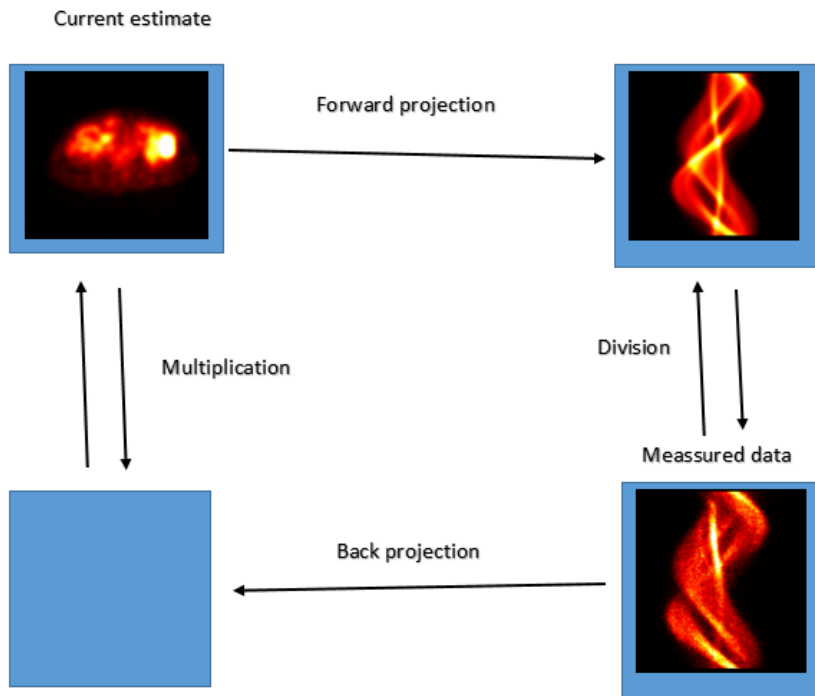

Figure 2. Schematic figure of the MLEM reconstruction algorithm. It is the forward projection that is based on Monte Carlo simulations.

2 AIM

The aims of this project were to develop novel methods and tools for analysis and quantification in nuclear medicine images. An additional aim was to collect these methods and tools into a novel, flexible and robust image platform for use in medical image research. The specific aims were:

2.1 Paper I

To develop a segmentation analysis method for SPECT images and to use it to study the impact of the background ROI in two planar kidney dosimetry methods.

2.2 Paper II

To develop a novel automatic image-based two-compartment model for bone marrow dosimetry, and to investigate its correlation to haematological response.

2.3 Paper III

To develop a novel statistical segmentation analysis algorithm for automatic detection of liver tumours in SPECT images, and to study its utility in a retrospective clinical study with ^{111}In-DTPA-octreotide for diagnosis of neuroendocrine liver tumours.

2.4 Paper IV

To develop a novel and fast Monte Carlo-based reconstruction algorithm for SPECT, and to compare its performance with clinically established reconstruction methods.

3 MATERIALS AND METHODS

The user interface for PhONSAi was written in c++.NET in visual studio. The database where the information of all images is stored is an SQLEXPRESS database. The Digital Imaging and Communication in Medicine (DICOM) server in PhONSAi was written in c# and is based on the mDICOM library. Visualization toolkit, VTK, was used for most of the visualization in PhONSAi. Most of the heavy algorithms are parallelised and written in CUDA and therefore executed on the GPU. CURAND was used for parallel pseudo random number generation and CUFFT was used for the parallel fourier transforms. All of the CUDA kernels were specifically written for this project. The thrust library included in the CUDA SDK is used for optimized parallel reduction on the GPU.

3.1 Paper I

The purpose of the first paper was to develop a method that could be used to investigate the influence of the background ROI on the quantification of the activity concentration in the kidneys. For this purpose an automatic image analysis method of SPECT images was constructed and implemented into PhONSAi. The method started by delineating the whole body and the kidneys using a level set segmentation algorithm (3.3.3). Then, the kidneys were projected to a 2D posterior projection, this image was named A. To locate the background ROIs at different positions around this projected kidney, a dilate algorithm was used. This algorithm was first run twice to position the ROIs two pixels away from the kidney border in image A. This new image was saved as B. For obtaining ROIs with a certain dimension, in this case a four pixel wide ROI, the dilate algorithm was executed 4 more times. This dilated area was subtracted by image B and saved as image C. Image C was then a 4 pixel wide area around the kidney with spacing 2 pixels to the kidney. C was divided into 10 parts, each part occupying an angle of 36 degrees from the centre of the kidney. These parts were now the 10 background ROIs around the kidney. Each of the 10 backgrounds ROIs and the kidney ROI was back projected through the SPECT volume to create column VOIs through the SPECT image (Figure 3). All voxels that were outside the body and in the kidney was set to 0.
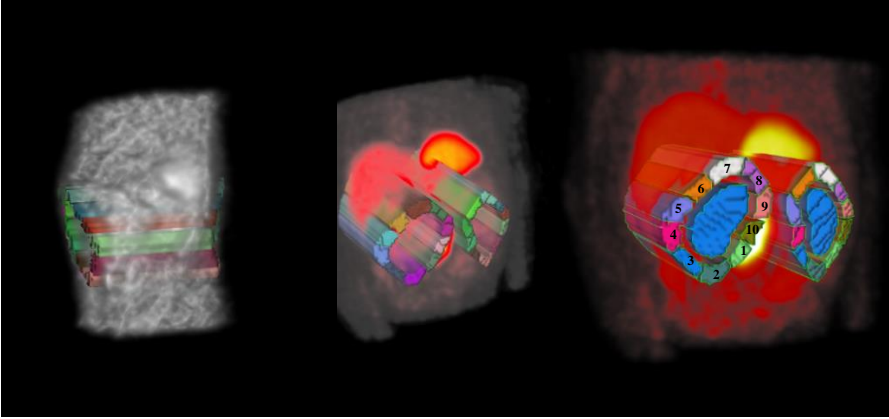
Figure 3. The backprojected kidney and background VOIs.

The activity concentrations in the background ROIs were compared to the true activity concentration in the background, as measured in the created column VOI in the SPECT image. From the SPECT image attenuated AP and PA projections were created, which generated the counts in the kidney and in the 10 background ROIs. These ROIs were then used to determine the activity concentration (*Ac*) in the kidney by both the posterior view (PostV) method (Eq. 3) and conjugate view method (Eq. 4), which was compared with the true activity concentration.

$$Ac_{PostV} = \frac{C_P}{volume} \cdot e^{\mu \cdot n_d} \cdot \frac{n_t \cdot \mu}{1 - e^{-\mu \cdot n_t}}$$

Eq. 3

$$Ac_{ConjV} = \frac{\mu \cdot n_t \cdot \sqrt{C_A \cdot C_P}}{e^{-\frac{\mu \cdot p_t}{2}} \cdot \left(e^{\frac{\mu \cdot n_t}{2}} - e^{-\frac{\mu \cdot n_t}{2}}\right) \cdot volume}$$

Eq. 4

C_A and C_P are the net counts in the AP and PA projections respectively and μ is the effective attenuation coefficient for ^{177}Lu in water. n_d, n_t and p_t are kidney depth (the distance between the patients back and the kidney), kidney thickness and the patient thickness respectively and *volume* is the volume of the kidney.

3.2 Paper II

In Paper II the aim was to develop a planar image-based method for estimation of the bone marrow dose. The basic idea was to assume that the low activity concentration in the whole body corresponds to non-physiological uptake in organs and that it is linearly related to the activity concentration in bone marrow. Thereby we developed an automatic algorithm for dividing the whole body into high- and low-uptake areas. In this algorithm a geometric mean image is first created from the anterior and posterior 2D images. Then a threshold-based whole body segmentation is performed and the number of uptake foci (NUF) is counted with a CCL algorithm (3.3.4) for each threshold value (named threshold index – ThI). A normalised NUF versus ThI (nNUFTI) curve (3.3.5) is acquired in the segmented whole body area, see Figure 4. The threshold value corresponding to the ThI at nNUF=0.1 is used to separate tissue
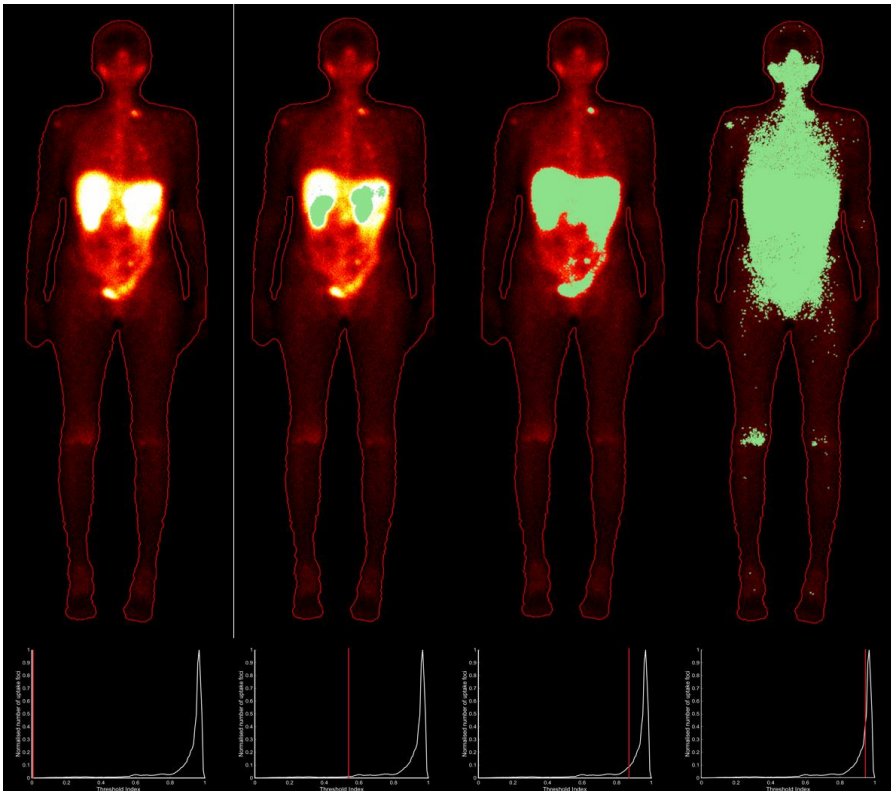

Figure 4. A region of interest of the whole-body. The number of uptake foci is calculated for different threshold values starting at the lowest ThI (A) and moving higher (B, C and D).

bound activity from activity in the blood. This nNUF value was based on best visual separation of the high and low uptake areas.

The activity concentration in the two compartments was determined by the conjugate view method (Eq. 2). The patient thickness was measured in the abdomen area in a high resolution CT image and used as the thickness of the high-uptake area. The thickness of a general organ, which was assumed to accumulate the activity in the high uptake area, was determined to 8 cm by measurements in a series of SPECT images. The weight of the high-uptake compartment was determined assuming a density of 1 and the volume calculated from the high-uptake compartment area and the abdominal thickness. The activity was assumed to be uniformly distributed in the low-activity compartment. The thickness of the low-activity compartment Pt_{low} was determined as:

$$Pt_{low} = \frac{W_{patient} - W_{high}}{A_{low}} \cdot \frac{1}{\rho}$$

Eq. 5

$W_{patient}$ is the weight of the patient, W_{high} is the weight of the high-uptake compartment and A_{low} is the area of the low uptake compartment. The assessed cumulated activity in the tissue in the foreground and background in the 2D image of the high-uptake compartment was added to the low-uptake compartment. For the low-uptake compartment a bi-exponential curve was fitted to the data when four data points (i.e. gamma camera measurements performed at 2h, 24h, 2 days and 7 days p.i.) were available and a mono-exponential curve fit was used when we had three data points (Figure 5). The curve fit to the data points from the high-uptake compartment was made with a linear fit between the first two data points and a mono-exponential function
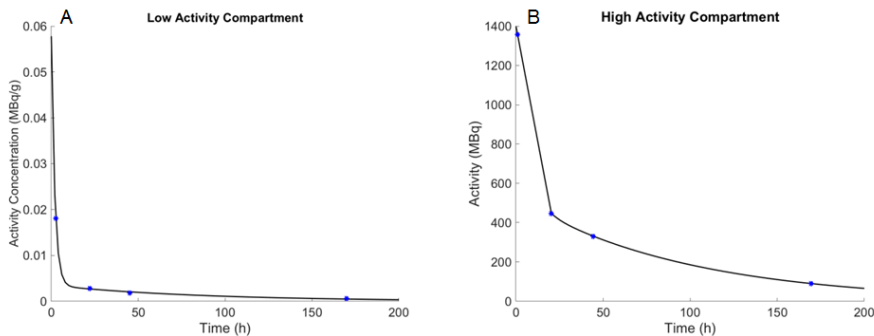

Figure 5. A bi-exponential curve fit for the low-uptake compartment (A) and a linear/mono-exponential curve fit for the high-uptake compartment (B).

to the rest. The cumulated activity was calculated by integrating the curves from t=0 to infinity.

The dose to the bone marrow was calculated:

$$D_{bm} = \tilde{A}_{bm} \cdot S_{bm \leftarrow bm} + \tilde{A}_{high} \cdot S_{bm \leftarrow high} \cdot \tilde{A}_{low} \cdot S_{bm \leftarrow low}$$

Eq. 6

$\tilde{A}_{bm}$ was derived from $\tilde{A}_{low}$, see below, and the S values were acquired from the RADAR website [23]. $S_{bm \leftarrow high}$ was calculated as a weighted mean of the S-values for liver, spleen and kidneys to the bone marrow and $S_{bm \leftarrow low}$ was calculated as the mean S-value for muscle and bone.

The Monte Carlo code SARec, described in 3.4.1, was used to determine the recovery correction factor. The ratio of activity concentration between the bone marrow and the low uptake compartment was determined by measuring it in 53 SPECT/CT images of 15 patients. The mean value of these ratios was used to adjust $\tilde{A}_{bm.}$

Haemoglobin (HB), white blood cells (WBC) and platelet (PLT) counts were measured in blood samples every other week during treatment and the calculated mean absorbed bone marrow dose was correlated to HB, WBC and PLT counts.

3.3   Paper III

In paper III the aim was to develop an automatic method for detection of liver tumours in SPECT images and test the methodology in a retrospective study with ^{111}In-DTPA-octreotide for diagnosis of neuroendocrine liver tumours. Since the focus was the detection of liver tumours, the liver was outlined by semi-automatic segmentation in the SPECT or CT. The tools used for segmentation of the liver were a threshold-based segmentation algorithm, a region growing algorithm, a level set algorithm and a manual VOI drawing tool. Details of these tools are described below and thereafter the automatic method for detection of liver tumours is described.

3.3.1   Threshold-based segmentation

For the threshold-based segmentation a threshold value is defined. If the voxel value is higher than or equal to the threshold value the voxel is included. This is easily done in parallel. The labelling of the included voxels is independent of order. The volume that is going to be segmented is copied to the GPU memory. A CUDA kernel that sets the voxel value to 1 if the current voxel

value fulfils the criteria and 0 otherwise is launched. The threshold-segmenting CUDA kernel is launched with the same number of threads as the total number of voxels. The data is copied back from GPU to RAM.

3.3.2 Region growing algorithm

The region growing starts with a number of voxels and iteratively includes neighbouring voxels that meet certain criteria until no more voxels are included. Input parameters are an initial segmentation, μ and a, where μ is the mean voxel value of the voxels included in the initial segmentation and a is a tolerance factor. The initial segmentation is often a small sphere of voxels. The criterion for a neighbouring voxel to be included in the segmentation is that its value belongs to the range [μ-aσ, μ + aσ], where σ is the standard deviation of the initial segmentation. This is a little bit tricky to do in parallel. This is how it is done in PhONSAi:

Memory is allocated on the GPU for input and output. All voxels in the output are set to 0 in parallel. The image to be segmented is copied to input data on the GPU. A CUDA kernel is launched with the same number of threads as the number of voxels, N. Each voxel in the input data is set to 1 if its value is in the range [μ-aσ, μ + aσ], otherwise 0. Memory for a 32-bit integer is allocated on the GPU and the pointer to that address is called nUpdate. nUpdate is set to 1. A while loop with the criterion that nUpdate > 0 sets nUpdate to 0 and launches a CUDA kernel with N threads. In the kernel: If output> 0 and input> 0, input it set to 0 and output is set to output + input of neighbours and nUpdate increased by 1. As this occurs simultaneously throughout the voxel matrix, multiple threads may add to nUpdate at the same time, which may result in wrong value of nUpdate. This is of no significance because nUpdate is only used as a binary criterion for the while loop. After the while loop has finished the output is thresholded in parallel so that all voxel values > 0 is set to 1 and the rest to 0. The output data is then copied to RAM.

3.3.3 Level set algorithm

The level set segmentation algorithm starts from an initial segmentation, which might be a result from another algorithm, a sphere or a manually drawn VOI.

The segmentation Γ is viewed as a level set of a function of a higher dimension.

$$\Gamma(\boldsymbol{x}, t) = \{\phi(\boldsymbol{x}, t) = 0\}$$

Eq. 7

Γ is manipulated implicitly through the level set function ϕ. The level set equation (Eq. 8):

$$\frac{\partial \phi}{\partial t} = -v|\nabla \phi|$$

Eq. 8

describes how ϕ changes with t. v is the velocity function and it is a function of the data to be segmented.

$$v = \left(a * S(I) + (1-a)\nabla \frac{\nabla \phi}{|\nabla \phi|} \right)$$

Eq. 9

$$S(I) = b - |I - T|$$

Eq. 10

$$\frac{\partial \phi}{\partial t} = -|\nabla \phi| \left(a * S(I) + (1-a)\nabla \frac{\nabla \phi}{|\nabla \phi|} \right)$$

Eq. 11

$$\phi(t + \Delta t) = \phi(t) + \Delta t \cdot v \cdot |\nabla \phi|$$

Eq. 12

Δt, a, b, T, $\phi(0)$, I and the number of iterations are the input parameters for the level set segmentation algorithm in PhONSAi. Δt is the time step for each iteration, a is a weight between the curvature and the velocity, b is the width of the threshold voxel value interval and T the centre. I is the image to be segmented. Memory is allocated for $\phi(x,t)$ and for $S(x)$. All voxels in S are created in parallel from the image I, b and T. In every iteration ϕ is updated in parallel according to Eq. 12. After all iterations the segmented closed surface is:

$$\Gamma(x) = \{\phi(x) = 0\}$$

Eq. 13

And the voxels that are inside that surface fulfils:

$$V(x) = \{\phi(x) \geq 0\}$$

Eq. 14

3.3.4   Parallel Connected Component Labelling

The parallel counting algorithm, the connected component labelling (CCL), sets each voxel value to its index if it is above the threshold value and to zero if it is below. A global Boolean variable called notFinished is set to true. A while loop with the condition notFinished is started. In the beginning of the loop the notFinished variable is set to false. A CUDA kernel called scan is launched with as many threads as there are voxels.

The scan kernel stores a variable called label from the voxel matrix at the current thread index and checks if it has a value above zero. If it has, a comparison between its value and all neighbouring voxels' nonzero values is performed. The voxel with the index equal to the variable label gets a new value equal to the minimum of its old value and the minimum in the comparison described above. The notFinished variable is set to true.

Another CUDA kernel that finds the root label and replaces the current label with the root in each connected region is launched with the same number of threads. This is performed as long as notFinished is true. After the while loop a parallel sorting algorithm in the thrust library is used to sort the label array in ascending order. The number of connected regions is acquired using the function thrust::unique on the sorted label array. Thrust::unique is a function that counts all the times a value changes from the beginning to the end in an array, i.e. the number of uptake foci is counted. The above algorithm is performed 125 times to receive the nNUFTI-curve (3.3.5). This number of times could be arbitrary set, but should be at least 100 to obtain satisfactory resolution.

3.3.5   nNUFTI

When the liver is segmented the maximum voxel value is found in the liver. 125 evenly spaced threshold values between 0 and the maximum value are generated and for each threshold value all voxels above the threshold value are set to 1 and the others to 0. For each threshold value the GPU-based CCL described above is used to count the number of connected foci and to calculate their sizes by histogram of the labels. When there is at least one focus of the size of at least two voxels the loop is terminated and the threshold value is saved as C_{max}. Now 125 new numbers are created evenly spaced from the saved threshold and 0 and for each of these the number of connected foci is plotted against the threshold index, ThI, which is defined as:

$$ThI = \frac{C_{max} - C}{C_{max}}$$

<div align="right">Eq. 15</div>

where C is the current threshold value. The curves produced according to the above described algorithm is normalised by the maximum number of connected uptake foci (nNUF). The nNUF vs ThI (nNUFTI) characteristic is used to determine tumour involvement, as described in 3.3.6.

3.3.6   Patient study

The nNUFTI method was tested in a retrospective study with 53 patients that were assessed as octreoscan negative and 10 patients that were octreoscan positive. The patients were randomly selected from the database. A 3-year follow up of the 53 octreoscan-negative patients divided the group into two subgroups. The patients who were found to have developed tumours in the liver during follow up were placed in one group and the patients who remained healthy after three years of follow up in another group. 40 patients ended up in the healthy group and 13 in the group with later demonstrated liver tumour involvement. To determine where and how the nNUFTI curve should be used to distinguish healthy livers from livers with tumour involvement, the curves from the 40 healthy patients and the 10 patients with confirmed tumour involvement were analysed. It was found that there was a clear correlation between ThI and mean voxel value in the liver, consequently the ThI was corrected for this effect. This corrected ThI is the nThI, normalised threshold index. The analysis read the nNUFTI curve where the difference between the healthy and the malignant was most statistically significant (Figure 6).
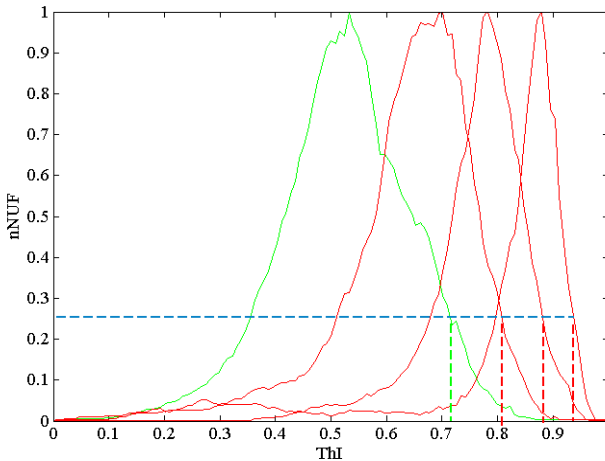
Figure 6. Example of nNUFTI curves of healthy (green) and malignant (red) livers with the markers at nNUF=0.25.

3.4 Paper IV

3.4.1 GPU-based Monte Carlo

In the last study, Paper IV, the aim was to develop a fast Monte Carlo method and use it in SPECT reconstructions. This Sahlgrenska Academy reconstruction (SARec) code was implemented into PhONSAi. SARec is written in CUDA for optimal speed and it assumes two 3D voxel matrices. One as the source where the voxel values correspond to activity concentration and one as the phantom where the voxel values are correlated to the atomic composition. The voxel values in the phantom should be in Hounsfield units, HU. The voxel sizes, the voxel dimensions and the origins of the matrices are passed as parameters. Furthermore, the number of photons per source voxel, an arbitrary number of photon energies and the corresponding branching ratios are passed as parameters.

The detector consists of a 2D matrix with arbitrary pixel sizes and a specific position in space. The crystal in the detector has specific spatial and energy resolutions, described by full width at half maximum (FWHM). The collimator is based on an angular response function (ARF) and a scattering kernel, which includes the scattering in the detector, i.e. the collimator, crystal, shielding and electronics. The ARF in SARec is based on cylindrical shaped collimator holes where the holes, due to septal penetration, are increased from their true sizes. The size of the collimator holes, and the values for the parameters of the scattering kernel were determined by gamma camera measurements of line

sources. Cross sections for energies between 10-600 keV in 24 atomic compositions are acquired from NIST XCOM [24]. A table that correlates HU to atomic composition and HU to density is created [25]. The ARF is calculated on the GPU in parallel for the selected collimator parameters and for 1000 angles between 0 and θ_{max} (Eq. 16-Eq. 18).

$$\theta_{max} = \text{atan}\left(\frac{D_{eff}}{L}\right)$$

Eq. 16

$$d = L \cdot \tan(\theta)$$

Eq. 17

$$ARF(\theta) = \frac{4 \cdot D_{eff}{}^2 \cdot \text{acos}\left(\frac{d}{D_{eff}}\right) - d \cdot \sqrt{D_{eff}{}^2 - d^2}}{\pi \cdot D_{eff}{}^2}$$

Eq. 18

where D_{eff} is the collimator effective hole diameter and L is the hole length. The Klein Nishina integral (Eq. 19) over 4π, σ_c, is calculated for 590 energies between 10 and 600 keV in parallel (Eq. 20).

$$\sigma_c = \int \frac{r_e^2}{2} \frac{1}{[1 + \gamma(1 - cos\theta)]^2}\left(1 + cos^2\theta + \frac{\gamma^2(1 - cos\theta)^2}{1 + \gamma(1 - cos\theta)}\right) d\mathbf{\Omega}$$

Eq. 19

$$\sigma_c = 2\pi r_e^2 \left\{\frac{1 + \gamma}{\gamma^2}\left[\frac{2(1 + \gamma)}{1 + 2\gamma} - \frac{1}{\gamma}\ln(1 + 2\gamma)\right] + \frac{1}{2\gamma}\ln(1 + 2\gamma) - \frac{1 + 3\gamma}{(1 + 2\gamma)^2}\right\}$$

Eq. 20

γ is the energy divided by 511 keV. All tabulated data are stored in the global memory on all the GPUs and bound to texture memory for performance issues. These tables are from now on read only and hardware linear interpolation is used.

Memory for the phantom, the source, and the resulting image is allocated on and copied to all of the GPUs. To avoid unwanted correlations between random numbers when generating random numbers in parallel, as many random number generators are initialised with unique seeds as the maximum number of parallel photons that are created on the GPUs. There are two parallelism options in SARec: either all the photons emitted from one voxel are simulated in parallel or one photon emitted from each voxel in the matrix are simulated in parallel. The former is to prefer when the source contain few voxels, as in the case for simulation of tumours into to the raw data set. The latter is to prefer for simulation of photon emission from large matrix dimension, as is the case

in the simulation of the forward projection in MC-based SPECT reconstruction.

The number of GPUs in the system, N_{GPU}, is acquired from the driver. N_{GPU} number of CPU threads are created, where each CPU thread handles one projection on one GPU. The main thread is delegating work to the other CPU threads until all projections are created.

The phantom and the source are rotated into the correct angle for the projection. The rotation is done in parallel and the time it takes is negligible. A CUDA kernel with N_{voxel} parallel GPU threads is launched where each thread is simulating one photon. This is done N_{photon} times.

The random number generator is copied from global to local memory. The photon's starting position is randomized uniformly in the source voxel. If the selected isotope has more than one energy peak, a uniform random number is used to determine at which index of the energy array the energy and corresponding weight should be read. The photon's initial direction in spherical coordinates φ and θ is sampled according to $\varphi = 2\pi r_0$ and $\theta = \mathrm{acos}(1 - r_1(1 - \cos(\theta_{max})))$. $\theta_{max} = \pi$. As long as the photon is inside the phantom and has an energy above 10 keV, it is given a new step to travel (s) by the use of the delta scattering method [26]:

$$s = -\frac{\ln(r)}{\mu_{max}}$$

Eq. 21

where μ_{max} is acquired from the table of attenuation coefficients at the current energy and the atomic composition of the maximum CT value. The total relative attenuation coefficients for Compton scattering, photo absorption and Rayleigh scattering are acquired at the current energy and atomic composition of the CT value where the photon arrives. If a uniform random number is less then $\frac{\mu}{\mu_{max}}$, an interaction occurs, otherwise a new step is sampled. If interaction occurs, another uniform random number determines which kind of interaction. If photo absorption, the photon is terminated; if Compton, a new direction and energy are sampled according to Kahn's rejection method [27]. To sample the new direction after a Rayleigh scattering, the following method is used:

$$\frac{d\sigma_{rayleigh}}{d\mathbf{\Omega}} = F^2(q,z)\frac{d\sigma_{thomson}}{d\mathbf{\Omega}}$$

Eq. 22

where F is the atomic form factor, which has been calculated and tabulated [28]. From the table of normalised integrated squared form factor, the value of q is sampled. The scattering angle is then calculated:

$$\theta = 2\,asin\left(\frac{qhc}{e}\right)$$

<div align="right">Eq. 23</div>

where h is Planck's constant, c is the speed of light in vacuum and e is the energy of the photon. The Thomson cross section is calculated by:

$$\sigma_{thomson} = \frac{r_e^2}{2}(1 + cos^2\theta)$$

<div align="right">Eq. 24</div>

where r_e is the classical electron radius.

A new uniform random number r between 0 and 1 is compared to the normalised $\sigma_{thomson}$. If r is smaller than the normalised $\sigma_{thomson}$, θ is selected, otherwise a new q is sampled and the procedure is repeated.

When the photon arrives at the detector, a uniform random number is compared to the ARF at the current incident angle. If the random number is smaller than the ARF, the photon is terminated. Two normal random numbers with mean=0 and FWHM of the crystal are used to adjust the position of the interaction point. Another normally distributed random number with the same FWHM as the energy resolution of the system is used to adjust the energy of the photon. If the photon's energy is inside any of the selected energy windows, the resulting image adds the value one in the point of interaction.

In pure MC code only around 1 of 10000 photons contributes to the resulting image. Such an approach is useful when the simulation of correct noise characteristics is of importance. This might be useful for simulation of tumours in SPECT raw data from healthy patients and to produce SPECT raw data from a digital source and phantom for other studies, but in MC-based SPECT reconstruction, where the forward projection is simulated, the noise should be as low as possible. In SARec some variance reduction techniques are used for reducing the simulation times and the noise level. Above the time-reducing methods by the ARF with the associated scattering kernel and the delta scattering method have been described. Below the use of scattering order and forced detection is described.

In Figure 7 the implementation of the scattering order technique is schematically described. First, a uniform random number between 0 and the

maximum number of interactions determines the scattering order of the photon. The maximum scattering order used in paper IV was 3, but the number can be arbitrarily chosen. Initially, the photon's weight is the activity concentration in the source voxel times the maximum number of interactions + 1. If the scattering order is 0, the photon is forced towards the detector with a randomly selected angle that is smaller than the maximal angle θ_{max} (Eq. 16) and its weight is multiplied with $(1 - cos\theta_{max})/2$. The photon is travelling towards the detector according to the delta scattering method, but at every step (s), before the interaction in the crystal, the photon's weight is multiplied by the probability (p) not to interact:

$$p = (1 - \frac{\mu}{\mu_{max}})$$

Eq. 25

When the photon arrives at the detector, the photon's weight is multiplied with the ARF for the corresponding angle.

If the scattering order is 1, the photon is launched isotropically and forced to interact inside the phantom. The distance d_v to the edge of the phantom's voxel matrix is measured along the photon direction, and the sampled path is:

$$s = \frac{-\ln(1 - r \cdot (1 - e^{-d_v \cdot \mu_{max}}))}{\mu_{max}}$$

Eq. 26

The present photon's weight (wht_p) is multiplied by the probability that interaction in the phantom matrix occurs, giving a new weight

$$wht_p = wht_p \cdot (1 - e^{-d_v \cdot \mu_{max}}) \cdot \frac{\mu}{\mu_{max}}$$

Eq. 27

where the last term is applied due to the use of the delta scattering method, μ is the attenuation coefficient at the point of interaction and the current energy. Thereafter, a Compton interaction is forced and the scattered direction is forced towards the detector. The new photon energy is given by Eq. 28.

$$hv' = \frac{hv}{1 + \gamma(1 - cos\theta)}$$

Eq. 28

With the scattered angle and the new energy, the differential Compton cross section is calculated (Eq. 30). The weight of the photon is multiplied with this cross section, divided by the integral of Klein Nishina over 4π (the

precalculated σ_c for the current energy) and multiplied with the forced solid angle. The photon is then travelling towards the detector, as described for scattering order 0.

$$\frac{d\sigma}{d\Omega} = \frac{r_e^2}{2} \frac{1}{[1+\gamma(1-cos\theta)]^2} \left(1 + cos^2\theta + \frac{\gamma^2(1-cos\theta)^2}{1+\gamma(1-cos\theta)}\right)$$

Eq. 29

$$\frac{d\sigma}{d\Omega} = \frac{r_e^2}{2} \left(\frac{\nu'}{\nu}\right)^2 \left(\frac{\nu}{\nu'} + \frac{\nu'}{\nu} - sin^2\theta\right)$$

Eq. 30

ν is the frequency of the photon before interaction and ν' is the frequency after.

If the scattering order is 2 or higher, the photon is launched isotropically. Interaction is forced in the phantom and the photon weight is adjusted as described above. A Rayleigh or Compton interaction may occur. The new direction and energy are sampled as described above. This is done until there is only one interaction left. The last interaction will always be a Compton with the scattering angle directed against the detector, as for scattering order 1. When the current projection is finished it is copied from GPU memory to RAM.

SARec was used as the forward projector in an OSEM algorithm called SARec-OSEM. Phantom measurements and patient data were reconstructed with SARec-OSEM, ST-OSEM and RRC-OSEM. A comparison between the three algorithms was performed.
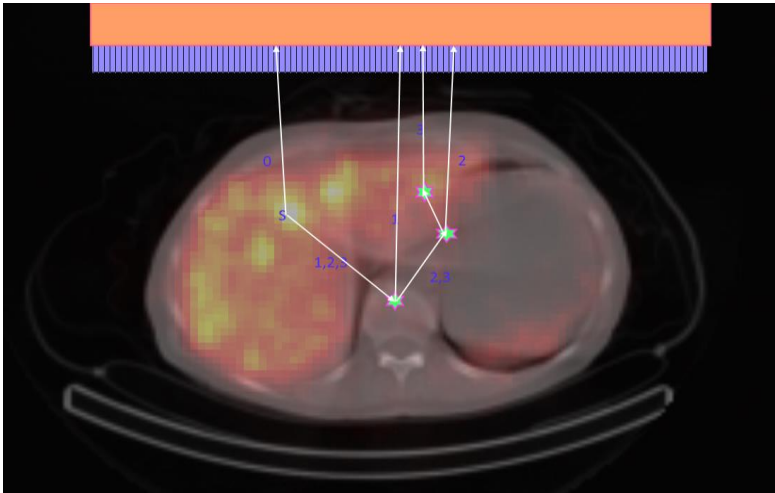
Figure 7. Schematic description of the variance reduction with a maximum scattering order of three. The photons originate from the source voxel S. Photons with scattering order 0-3 are shown in the figure. Photon 0 is emitted towards the detector, Photon 1 is forced to interact 1 time before it is forced towards the detector, Photons 2 and 3 are forced to interact 2 and 3 times, respectively, before they are forced to interact with the detector.

4 RESULTS

During the project time PhONSAi has developed into an advanced workstation with similar functionality as commercial workstations such as Xeleris (GE Healthcare, USA) and Hermes (Stockholm, Sweden), but with full user flexibility and control over the algorithms. PhONSAi has a DICOM server written in C# and SQL Server-based patient database. The user interface of PhONSAi is written in C ++.NET and the most computationally intensive algorithms are written in CUDA [29]. VTK [30], which is an open source library, has been used for most of the visualization. PhONSAi supports most medical image formats, i.e. most DICOM image formats, interfile, mhd and raw voxel values. The user interface has been developed together with the members of the research group to an intuitive and flexible user interface. The number of display windows, the number of images, the view in the display windows, and the size and structure of the display windows on the screen can be easily controlled by the user. In PhONSAi several different colour schemes are implemented. Additionally, the user can straightforwardly create new colour schemes. At present PhONSAi contains around 50 different image processing, segmentation and reconstruction algorithms, as well as the newly developed analysis methods, described above and used in Papers I-III. Furthermore, the Monte Carlo code for photon transport was implemented in PhONSAi. SARec can be used to simulate metastases in SPECT raw data and to create SPECT raw data from voxel-based sources and phantoms, but, above all, in this project SARec was used for iterative reconstruction as described above and in Paper IV.

4.1 Paper I

The algorithm created for studying the impact of the background ROI in two planar kidney dosimetry methods performed well. Once the parameters needed for the dosimetry was defined, the algorithm generated the same results for repeated executions, i.e. the algorithm was stable and precise. The ratio between the background VOIs and the true background varied between 0.36 and 2.08 for the right kidney and 0.44 to 1.52 for the left kidney. The variance between patients showed to be high for most of the background VOIs. The coefficient of variation (CV) ranged from 16 to 181% for the right kidney and from 16 to 70% for the right. The background with the highest accuracy, number 6 (Figure 8), had the mean quote to true background of 1.01, but the variance was high. The CV at number 6 was 47% and the number of negative net counts was 15% for the conjugate view method. The background with the lowest CV for both the left and right kidney was number 3, with a CV of 16%

for the right kidney and 15% for the left. The background-to-true background ratio (BTR) for number 3 was 0.36 for the right and 0.50 for the left.
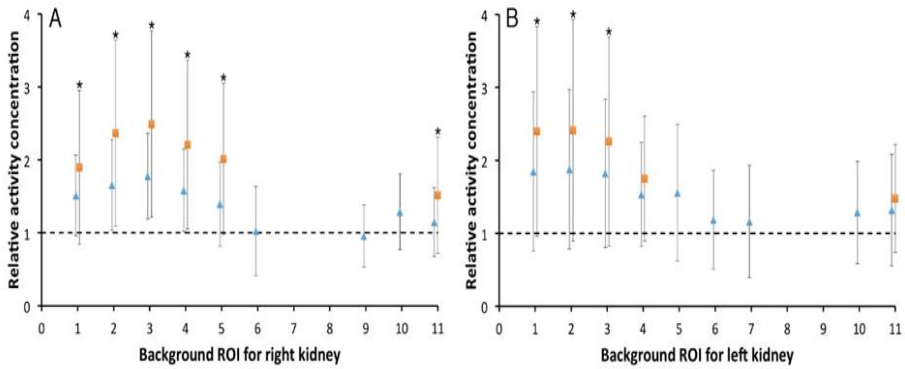

Figure 8. The relative activity concentrations in the background ROIs for the right (A) and left (B) kidneys. The orange squares are the relative activity concentration estimated with the ConjV method and the blue triangles the PostV method (reprinted from Paper I).

Calculations of the activity concentration in the kidneys were performed using both the ConjV method and the PostV method with all eleven backgrounds. The precision and accuracy of the ConjV method was overall poor. The background quotes (compared to the real activity concentrations, as determined from SPECT) ranged from 1.48 to 2.49 with a CV range from 39 to 70%. The PostV method generated improvement in accuracy and precision. The activity concentration was calculated with a significantly better accuracy with the PostV method for six background ROIs in the right kidney and four in the left compared to the ConjV method. The surrounding background ROI gave a quote to true activity concentration of 1.15 and 1.32 for the right and left kidneys respectively. The corresponding CVs were 41 and 58%.

4.2   Paper II

The developed image-based method for bone marrow dosimetry could be used on all patients and all images. The nNUFTI curve looked similar in all images and the selected value of nNUF=0.1 showed to be a good separator of the high and low uptake compartments. When the compartments were separated, the activity was quantified for both compartments at all time points. Time activity curves were created by fitting the low activity compartment with four points to a bi-exponential function, the low activity compartment with three points to a mono-exponential function and the high activity compartments to a combination of a linear and a mono-exponential function.

The median absorbed dose to the bone marrow in the patient group was calculated to 0.2 Gy per 7.4 GBq ^{177}Lu. The dominating contributor to the bone marrow dose was the self dose (85%). The cross doses from the high and low activity compartments contributed with 9 and 6%, respectively.

The calculated mean and total bone marrow doses were statistically correlated with the nadir value of HB, WBC and PLT during the treatment. The p values were below 0.01 for all correlations. The variance was high around the linear correlation; the r-value was between -0.45 and -0.36.

4.3   Paper III

The nNUFTI method performed well on all the patients included in the study. The nNUFTI curves showed a similar pattern in all healthy patients and a separable pattern in the livers with known metastases. The implementation of the algorithm in PhONSAi made it easy to use and gave a good visualization of the foci distribution in the liver (Figure 9).

The group of 53 octreoscan negative patients is called octreotide(-) and the group of patients with visible metastases in the liver is called octreotide(+). The patients that showed to have tumour involvement in the liver by any radiological techniques was placed in radtech(+) and the rest in radtech(-).

During follow up, 13 of the 53 patients showed metastases in the liver. The difference in nThI at nNUF=0.25 at the right side of the curve between these 13 patients and the other 40 healthy livers was statistically significant (p<0.01). 5 of the 13 had a ThI higher than the highest ThI in the group of the 40 healthy livers, see Figure 10. An error in the data processing was discovered after publication of paper III, which after correction increased the nThI for one of the patients so the number of detectable tumours increased from four to five.
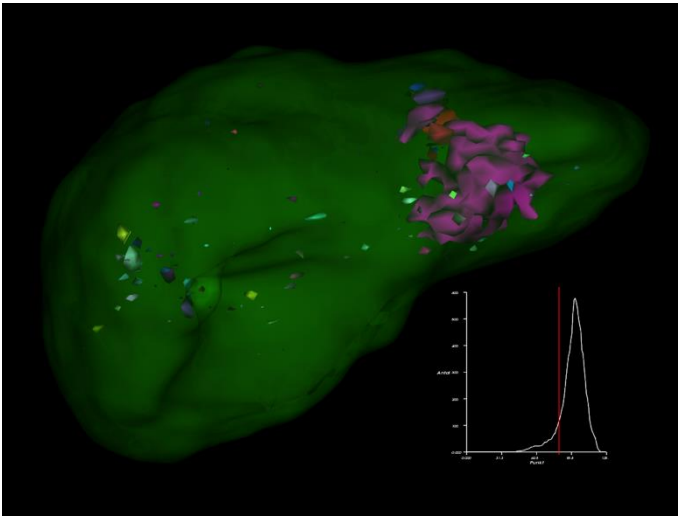
Figure 9. The nNUFTI curve in a liver with known metastases and corresponding visualization at a certain ThI (red line) (reprinted from Paper III).
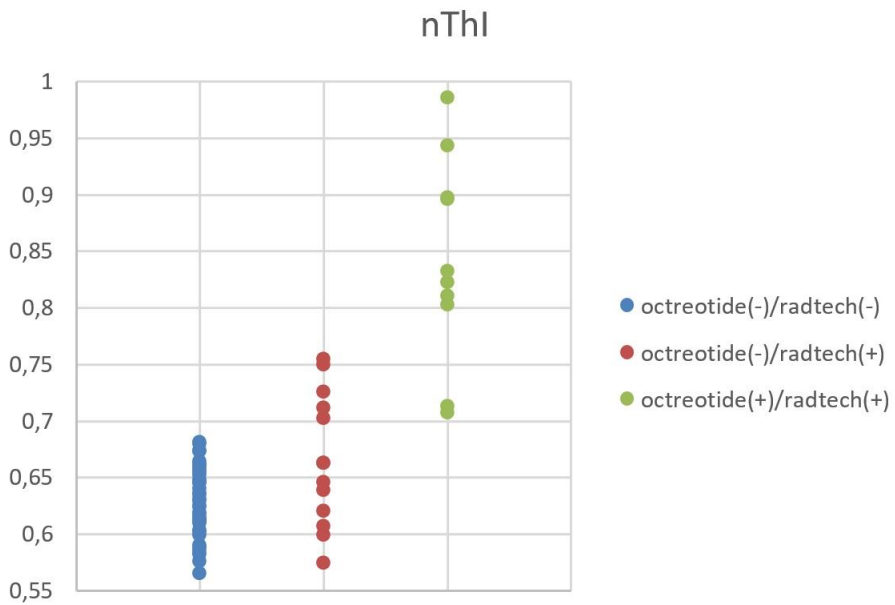

Figure 10. nThI at nNUF=0.25 for healthy patients (blue), patients with metastases in follow up (red) and patients with known metastases (green).

4.4 Paper IV

In SARec the number of energies in the source and corresponding branches can be arbitrary selected by the user. This means for example that bremsstrahlung spectra from ^{90}Y in tissue can be easily incorporated into SARec. ^{177}Lu, ^{99m}Tc, ^{111}In, ^{131}I, ^{123}I and ^{90}Y are predefined isotopes. However, in this project the angular response model of the detector was limited to ^{177}Lu.

The performance of SARec with a scattering order of 3 is around 2 billion photons per second. In the reconstruction algorithm each iteration requires around 100 billion photons to generate projections with acceptable noise levels for the SPECT reconstruction, which gives an iteration time of around 60s.

A profile perpendicular to a simulated line source was compared to a profile in a corresponding measured image (Figure 11). The agreement was within 5% based on comparison between integrals.

The signal to background ratio (SBR) for the largest sphere in the phantom was about 97% of the true SBR with SARec-OSEM, compared to 79% and 65% for RRC-OSEM and ST-OSEM reconstructions, respectively.

The SPECT data reconstructed with SARec-OSEM had a more accurate signal-to-background ratio and a higher resolution than RRC-OSEM and ST-OSEM (Figure 12). Phantom acquisitions showed that SARec-OSEM performed better, both quantitatively and visually, than its two competitors and SARec-OSEM also reconstructed patient SPECT images with higher image quality (Figure 13 and Figure 14).
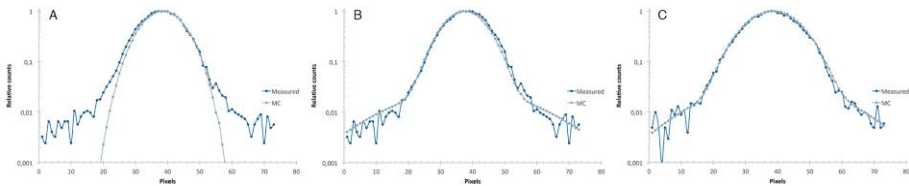

Figure 11. Simulation of line sources of ^{177}Lu revealed similar profiles as the measured line profiles. A) The ARF without scattering kernel agree well with the main intensities from the line source (observe the logarithmic scale) but could not capture scattering in the detector. B) Adding of the scattering kernel to the ARF also capture the photon scattering in the detector at 5 cm, and C) at 10 cm from the collimator surface.
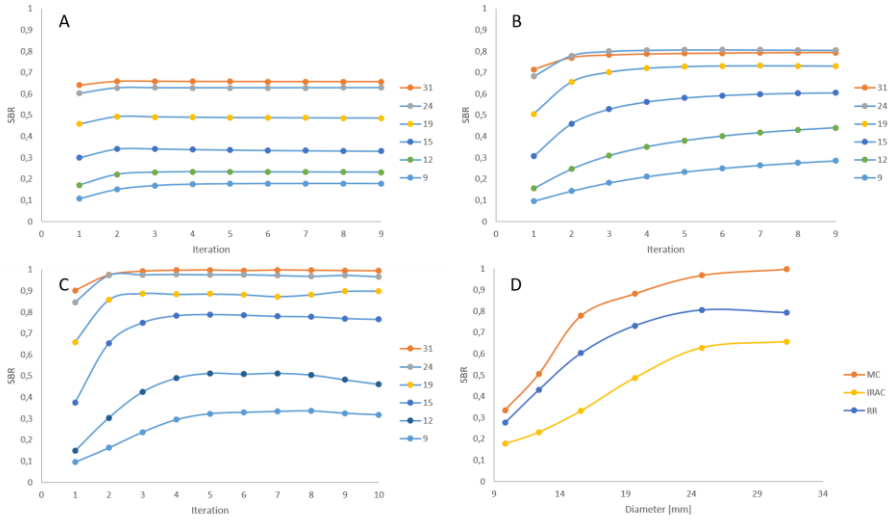
Figure 12. Signal to background as a function of the number of iterations for A) ST-OSEM, B) RRC-OSEM and C) SARec-OSEM. D shows signal to background as a function of sphere diameter for the three reconstruction algorithms with 5 iterations.
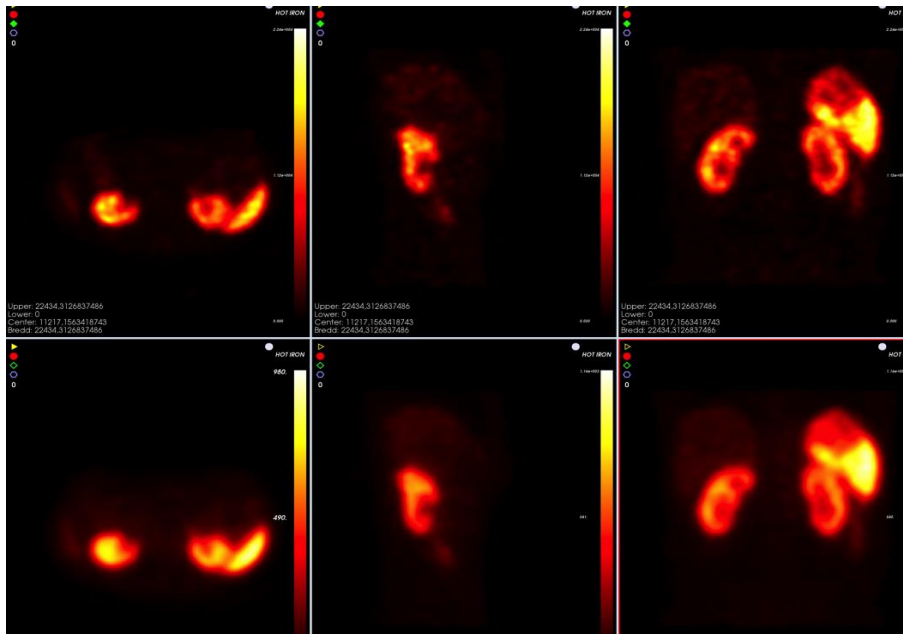
Figure 13. SPECT images of kidneys and spleen in three orthogonal planes. The upper SPECT is reconstructed with SARec-OSEM and the lower with ST-OSEM.
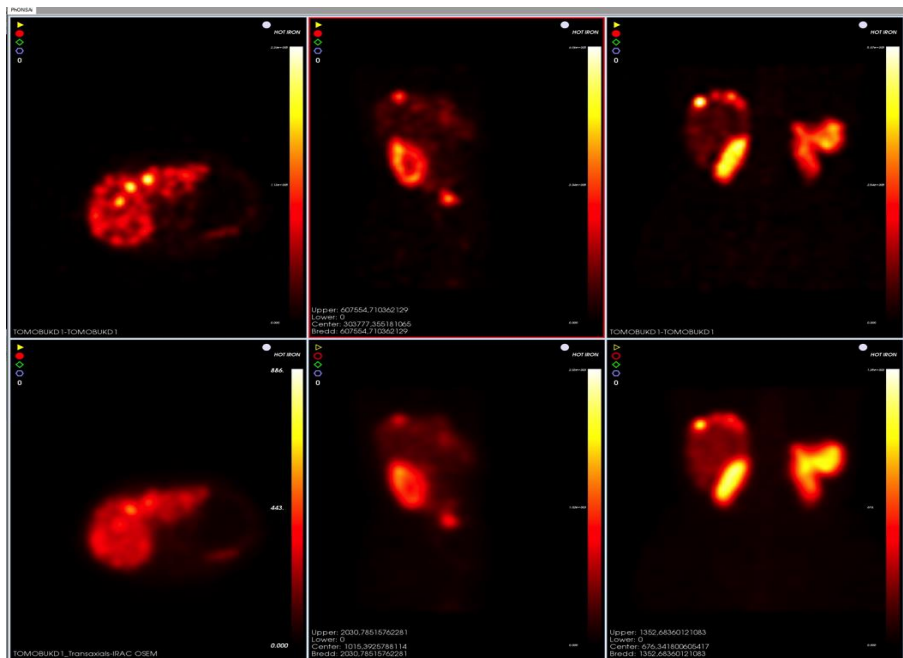

Figure 14. SPECT images of a liver with metastases. The upper SPECT is reconstructed with SARec-OSEM and the lower with ST-OSEM.

40

5 DISCUSSION

5.1 Paper I

Activity concentration estimation and dosimetry in 2D images are associated with large uncertainties. The results indicate that the anterior projection in most cases does not add any useful information to the kidney activity concentration estimate. The kidneys are often positioned closer to the patient's back, which, due to attenuation, will result in low signal in the anterior view projection of the kidney. The signal is in some cases close to zero after background correction. Using the conjugate view method in these cases may cause activity concentration estimates to be close to zero or result in a complex number. In the posterior view projection, signal originating from the organs and tumours that are located more anterior than the kidneys are more attenuated than the kidneys, and therefore does not interfere as much in the activity concentration estimate as it does in the conjugate view method. The problem with finding a background ROI to compensate correctly for the over- and underlying uptake can be solved by using SPECT, i.e. finding the most correct background ROI position for the individual patient by using the methodology developed in this study. One downside with SPECT is that the acquisition time is longer for the same statistics and FOV. If activity concentration estimates in the abdomen are the objective with the gamma camera acquisition, a better estimate might be obtained by acquiring a SPECT with the same acquisition time as the planar image.

If kidney dosimetry is performed by using planar images, this study indicates that it would be beneficial to use the posterior view method and place the background ROI around the kidney, where the CV was lowest. This will in most cases overestimate the activity concentration in the kidney, but this overestimate has to be further investigated by refined studies. This study assumed that the SPECT resulted in correct activity concentration estimate. However, SPECT is reconstructed from gamma camera projections, containing gamma camera blurring and scattering effects, which are propagated into the SPECT image. This will result in a blurred and scatter-influenced image, which in turn might influence the quantitative by some degree. Furthermore, we used an approximated method to estimate the attenuation coefficient from the CT, which is good enough for this estimate of the attenuation in the tissues above and under the kidneys, but would be less valid for regions with the attenuation coefficient much different from water such as lung and bone tissue. In this case the energy dependence of the attenuation coefficients might yield a less valid estimate of the lung and bone attenuation coefficients. Nevertheless, the

overall results, as described above, will be valid from our used methodology, but improvement can be used to correct for these effects. One way to correct for these effects is to integrate MC simulation of the forward projection in the reconstruction. Therefore, we initiate the SARec project which might be the best way to evaluate the influences of the image degrading effects that are present in Paper I.

5.2   Paper II

The calculated absorbed doses to bone marrow seem to be in the same order of magnitude as previously presented [11, 14, 15, 31-33]. Furthermore, the absorbed doses from this non-invasive method correlated with haematological toxicity, which is seldom observed with other methods. In the methodology a threshold value is used to separate the high activity area from the low activity area. That threshold value is obtained from the nNUFTI algorithm. This means that the area of the high activity area and the low activity area might vary at the different time points, which indicates that the methodology follows the redistribution over time. In contrast to thresholding from the whole body histogram, the nNUFTI algorithm also follows the spatial distribution of the pixel values by grouping them into segmented areas. If this methodology is superior to histogram analysis remains to be investigated. Another approach to divide the whole body into two compartments would be to use a fixed area either by using this methodology at one time point and adjust the resulting ROIs so they fit in the other images, or using this method at one time point and then iteratively find a threshold value that generates the same areas in the other images, or use a predefined individualised area for the high (or low) uptake compartment. All these methods might work but need to be developed. However, it might be questioned if these variants will have any beneficial value since the variance in the nNUFTI methodology is low and it has a correlation with haematological response.

More important is to combine nNUFTI with SPECT-based activity concentration determination in the bone cavity. With a Monte Carlo-based SPECT reconstruction, the activity concentration in the bone cavity may be measured with higher accuracy and precision. This will be studied with SARec-OSEM.

5.3   Paper III

The performance of the algorithm for detection of liver tumours in SPECT images increased significantly, with respect to calculation time, when it was

parallelised and run on the GPU. The results showed that the quantitative measure ThI read out at nNUF=0.25 at the right side of the curve separated healthy and malignant liver groups with the highest statistical significance. A tumour with a quite low tumour-to-normal concentration (TNC) located in a region of the liver where the normal tissue has high uptake will skew the nNUFTI curve towards higher ThI while a tumour with the same TNC located in a lower activity region in the liver only affects the ThI read out to the right of the peak. This in combination with less variation among the healthy livers on the right of the peak is the probable reason for better significance on the right side of the peak.

Simpler models, like quotes between max and mean voxel value, have been tested on this clinical material without success. A 100% separation between the groups was never expected, since some patients in the follow up group may have developed metastases after the SPECT was acquired and some patients may have metastases that do not overexpress somatostatin receptors [4]. The results of this study are interesting but further studies are needed to verify and determine its usefulness in other applications, such as PET imaging of e.g. ^{68}Ga-DOTATANOC [34]. A combination of nThI and the use of the visual nNUFTI tool in PhONSAi may be an interesting future application, which might have the potential to improve the success rate in octreoscan diagnosis of liver tumours.

5.4   Paper IV

The novel SARec methodology with a novel collimator model produced SPECT reconstructions with high image quality, i.e. the recovery resolution was improved over the state-of-the-art reconstructions with recovery resolution corrections. The visual inspection of clinical images also showed improvement with SARec-OSEM.

The collimator model in SARec is based on an ARF and a convolution with a scattering kernel. The model is fast and simple and quite accurate for the isotopes used in this thesis. The ARF of the collimator model does presently not take septal thickness or energy into account, but the hole diameter of the collimator is adjusted so that the simulated images match the measured and the two parameters of the scattering kernel (fraction and width) are adjusted to make the fit as good as possible. The downside with this approach is that calibrations against gamma camera images need to be performed for each collimator isotope combination. This makes the arbitrary collimator definition and arbitrary isotope definition meaningless. Another downside with this approach is that the ARF is independent of the azimuthal angle of the incoming

photon. This makes all points to be circular symmetric. The real collimators have hexagonal holes, which make the point spread function look like a star when the energy is high enough to penetrate the thin enough septum.

SARec is not only used for iterative SPECT reconstructions. SARec can also be used to create SPECT raw data from digital voxel-based sources and voxel-based phantoms (Figure 15) and it can be used to simulate metastases in clinical SPECT raw data (Figure 16). Simulating metastases in SPECT raw data can be useful when for example evaluating reconstruction algorithms of interest.

Further performance optimisation may increase the performance with respect to signal to noise per photon and number of photons per second. All of the launched photons will interact in the crystal but many will not contribute to the resulting image. If the photon energy is outside the energy window after it has been shifted with the FWHM of the crystal, it is terminated. The weight of the photon could instead be multiplied with the integral of the Gaussian of the photon, describing the energy resolution, over the energy window. Many photons interact in the air outside the body (Figure 17). Their weight is multiplied with the correct probability, but since the probability is extremely low and these photons are located outside the body, they will not contribute to the interesting part of the image.

The Monte Carlo code is run on NVIDIA's GeForce GPUs (NVIDIA, USA). The performance of 32-bit floating numbers is equal for the best GeForce and Tesla cards (NVIDIA, USA) but for double float the GeForce has a performance drop of 20 compared to a factor of 3 on the Tesla. For Monte Carlo applications where double precision is needed, Tesla GPUs should be used. Single precision floating point numbers are enough for the applications in this thesis [22].

The collimator model used in SARec is simple, since it requires a calibration. A more complex model that takes the photon energy, septal thickness and the azimuthal angle of the photon into account will be developed eventually [35]. However, this will require that the energy window is defined for the specific radionuclide and that the geometric shape of the collimator is modelled. In this way the initial idea that SARec would be a general MC code is lost, and it will become a radionuclide specific code for SPECT simulations. With this new direction of SARec future optimisation, such as changing the 4 pi

emission of the scattering photons to the maximal angle that have a probability to be registered in the detector, will be done in upcoming studies.
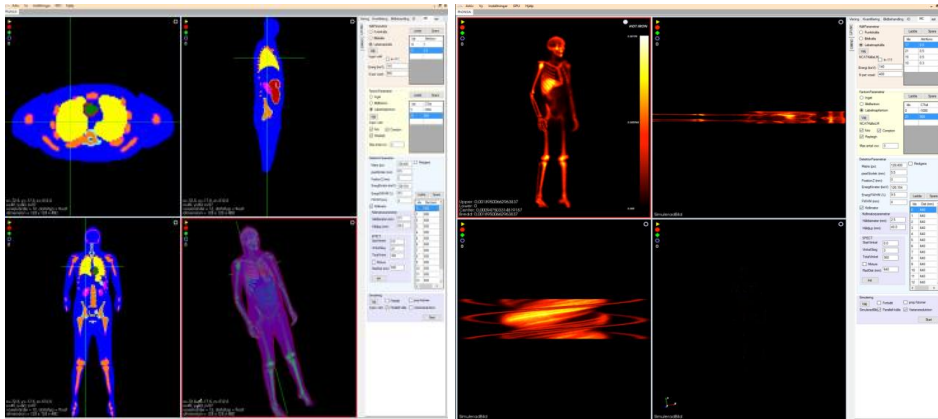

Figure 15. A) The SARec UI in PhONSAi with a label map ready to be filled with activity. B) A simulated SPECT from a source with activity in the liver and the skeleton.
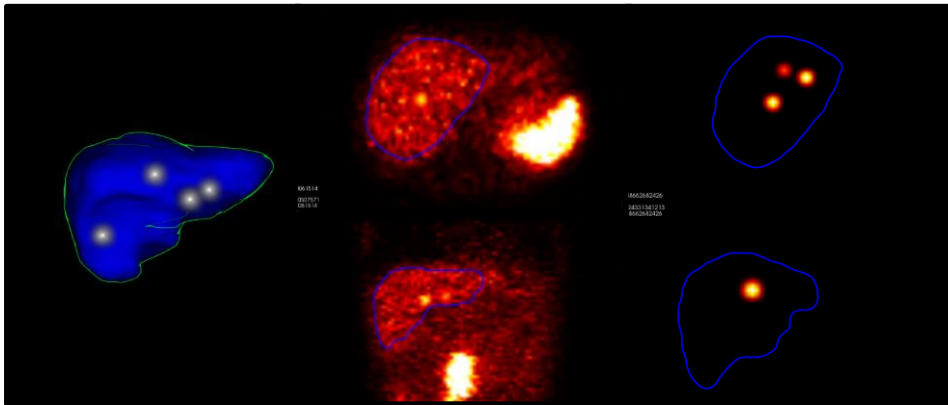

Figure 16. 4 metasteses are created in the liver VOI and simulated to the raw data and then reconstructed back to a 3D voxel matrix along with the rest of the SPECT data.

Figure 17. This is a simulated anterior projection of a lablemap source with activity in the skeleton voxels. The source is located in a water filled body phantom surrounded with air. It's the same image on the left and the right but the window and level are set different. The scattered photons in the body is visible on the left and all the insignificant scattered photons in the air are visible to the right.

6 CONCLUSION

PhONSAi is today a useful image platform for visualization, analysis, processing, reconstruction and quantification of medical images. It is used both clinically and in research.

6.1 Paper I

We conclude that the posterior view method gives higher accuracy than the commonly used conjugate view method when it comes to activity concentration estimates in the kidneys. The caudal position of the background ROI, and the surrounding background ROI, showed to vary least between the patients.

6.2 Paper II

The absorbed dose to bone marrow calculated with the two compartments method correlates well with haematological toxicity and it has about the same order of magnitude as blood based bone marrow dosimetry.

6.3 Paper III

The nNUFTI methodology for finding liver tumours showed high potential for being a useful method in the diagnosis of liver tumours with ^{111}In-octreoscan.

6.4 Paper IV

A fast and accurate Monte Carlo-based reconstruction algorithm for SPECT was developed. It performs better than the standard OSEM algorithm as well as the OSEM with resolution recovery correction. This novel approach of SPECT reconstruction might be worth to implement in clinical routine.

7 FUTURE PERSPECTIVES

One popular application of GPU power is CUDA-based deep learning or artificial neural network. It would be interesting to try to implement deep learning in PhONSAi. PhONSAi could be taught the difference between a healthy and a malignant liver. Deep learning has been proven to improve diagnosis of myocardial scintigraphy [36] and bone scintigraphy [37]. One downside with deep learning is that it requires very large learning data sets.

It would be valuable to continue the development of the nNUFTI algorithm for liver tumour detection. As it is today it is optimized for the clinical reconstructions parameters used at Sahlgrenska University Hospital. We could study how a combination of the visualization part of nNUFTI in PhONSAi and the quantitative measure ThI performs together against the standard method. It would be interesting to redo the nNUFTI study on the same material reconstructed with SARec. SARec could also be used to simulate metastases in the healthy group for studying the detection limits of nNUFTI, with the aim to improve the methodology.

The collimator model in SARec is based on the geometric shape of the collimator hole and use a scattering kernel for inclusion of photon scattering in the detector. It could be developed into a more sophisticated model, which may take septal penetration and scatter into account by simulating the ARF for various energies and thereby more correct accurate septal penetration for high energy photons can be modelled. We will continue to develop the Monte Carlo code and the reconstruction algorithm.

ACKNOWLEDGEMENT

And most of all I would like to thank my lovely and supporting wife **Isabelle**. You together with my children **Alva** and **Evert** are the meaning in my life. I love you!

REFERENCES

1. P, P., *Analytic and Iterative Reconstruction Algorithms in SPECT.* J Nucl Med, 2002. **43**: p. 1343-1358.
2. Morey, A.M. and D.J. Kadrmas, *Effect of varying number of OSEM subsets on PET lesion detectability.* J Nucl Med Technol, 2013. **41**(4): p. 268-73.
3. Tischler, A.S., *The dispersed neuroendocrine cells: the structure, function, regulation and effects of xenobiotics on this system.* Toxicol Pathol, 1989. **17**(2): p. 307-16.
4. Forssell-Aronsson, E., et al., *Biodistribution data from 100 patients i.v. injected with 111In-DTPA-D-Phe1-octreotide.* Acta Oncol, 2004. **43**(5): p. 436-42.
5. Search, T.L.L.N.D. and F. Version 2.0, *Table of isotopes decay data http://nucleardata.nuclear.lu.se/toi/nuclide.asp?iZA=490111.* 1999.
6. Robinson, A.P., et al., *The influence of triple energy window scatter correction on activity quantification for (1 7 7)Lu molecular radiotherapy.* Phys Med Biol, 2016. **61**(14): p. 5107-27.
7. Bernhardt, P., et al., *Dosimetric comparison of radionuclides for therapy of somatostatin receptor-expressing tumours.* Int J Radiat Oncol Biol Phys, 2001. **51**(2): p. 514-24.
8. Ljungberg, M., et al., *MIRD Pamphlet No. 26: Joint EANM/MIRD Guidelines for Quantitative 177Lu SPECT Applied for Dosimetry of Radiopharmaceutical Therapy.* J Nucl Med, 2016. **57**(1): p. 151-62.
9. Svensson, J., et al., *Renal function affects absorbed dose to the kidneys and haematological toxicity during (1)(7)(7)Lu-DOTATATE treatment.* Eur J Nucl Med Mol Imaging, 2015. **42**(6): p. 947-55.
10. Svensson, J., *Targeted radionuclide therapy for patients with neuroendocrine tumours.* 2016.
11. Bergsma, H., et al., *Subacute haematotoxicity after PRRT with (177)Lu-DOTA-octreotate: prognostic factors, incidence and course.* Eur J Nucl Med Mol Imaging, 2016. **43**(3): p. 453-63.
12. Cremonesi, M., et al., *Dosimetry in Peptide radionuclide receptor therapy: a review.* J Nucl Med, 2006. **47**(9): p. 1467-75.
13. Fleming, J.S., *A technique for the absolute measurement of activity using a gamma camera and computer.* Phys Med Biol, 1979. **24**(1): p. 176-80.
14. Bodei, L., et al., *Peptide receptor radionuclide therapy with (1)(7)(7)Lu-DOTATATE: the IEO phase I-II study.* Eur J Nucl Med Mol Imaging, 2011. **38**(12): p. 2125-35.
15. Sandstrom, M., et al., *Individualized dosimetry of kidney and bone marrow in patients undergoing 177Lu-DOTA-octreotate treatment.* J Nucl Med, 2013. **54**(1): p. 33-41.

16. Larsson, M., et al., *Estimation of absorbed dose to the kidneys in patients after treatment with 177Lu-octreotate: comparison between methods based on planar scintigraphy.* EJNMMI Res, 2012. **2**(1): p. 49.

17. Ezziddin, S., et al., *Outcome of peptide receptor radionuclide therapy with 177Lu-octreotate in advanced grade 1/2 pancreatic neuroendocrine tumours.* Eur J Nucl Med Mol Imaging, 2014. **41**(5): p. 925-33.

18. Sabet, A., et al., *Long-term hematotoxicity after peptide receptor radionuclide therapy with 177Lu-octreotate.* J Nucl Med, 2013. **54**(11): p. 1857-61.

19. Sgouros, G., *Dosimetry of internal emitters.* J Nucl Med, 2005. **46 Suppl 1**: p. 18S-27S.

20. Rahmim, A. and H. Zaidi, *PET versus SPECT: strengths, limitations and challenges.* Nucl Med Commun, 2008. **29**(3): p. 193-207.

21. Sohlberg, A.O. and M.T. Kajaste, *Fast Monte Carlo-simulator with full collimator and detector response modelling for SPECT.* Ann Nucl Med, 2012. **26**(1): p. 92-8.

22. Garcia, M.P., et al., *Accelerated GPU based SPECT Monte Carlo simulations.* Phys Med Biol, 2016. **61**(11): p. 4001-18.

23. RADAR, *http://doseinfo-radar.com.*

24. National Institute of Standards and Technology, G., MD., *http://physics.nist.gov/xcom*

25. Schneider, W., T. Bortfeld, and W. Schlegel, *Correlation between CT numbers and tissue parameters needed for Monte Carlo simulations of clinical dose distributions.* Phys Med Biol, 2000. **45**(2): p. 459-78.

26. Ljungberg, M., A. Larsson, and L. Johansson, *A New Collimator Simulation in SIMIND based on the Delta-Scattering Technique.* Nuclear Science Symposium Conference Record. 2004;6:3584-8., 2004.

27. Ljungberg, M. and S.E. Strand, *A Monte Carlo program for the simulation of scintillation camera characteristics.* Comput Methods Programs Biomed, 1989. **29**(4): p. 257-72.

28. Muhammad, W. and S.H. Lee, *New empirical equation for the atomic form factor function in the momentum transfer range, q=0-50 A(-1) for the elements in the range 1 </= Z </= 30.* PLoS One, 2013. **8**(8): p. e69608.

29. NVIDIA, *CUDA http://www.nvidia.co.uk/object/cuda-parallel-computing-uk.html.* 2016.

30. kitware, *VTK, http://www.vtk.org.* 2016.

31. Wehrmann, C., et al., *Results of individual patient dosimetry in peptide receptor radionuclide therapy with 177Lu DOTA-TATE and 177Lu DOTA-NOC.* Cancer Biother Radiopharm, 2007. **22**(3): p. 406-16.

32.   Jackson, P.A., et al., *An automated voxelized dosimetry tool for radionuclide therapy based on serial quantitative SPECT/CT imaging.* Med Phys, 2013. **40**(11): p. 112503.

33.   Forrer, F., et al., *Bone marrow dosimetry in peptide receptor radionuclide therapy with [177Lu-DOTA(0),Tyr(3)]octreotate.* Eur J Nucl Med Mol Imaging, 2009. **36**(7): p. 1138-46.

34.   Krausz, Y., et al., *68Ga-DOTA-NOC PET/CT imaging of neuroendocrine tumours: comparison with (1)(1)(1)In-DTPA-octreotide (OctreoScan(R)).* Mol Imaging Biol, 2011. **13**(3): p. 583-93.

35.   Song, X., et al., *Fast modelling of the collimator-detector response in Monte Carlo simulation of SPECT imaging using the angular response function.* Phys Med Biol, 2005. **50**(8): p. 1791-804.

36.   Lomsky, M., et al., *Evaluation of a decision support system for interpretation of myocardial perfusion gated SPECT.* Eur J Nucl Med Mol Imaging, 2008. **35**(8): p. 1523-9.

37.   Sadik, M., et al., *Computer-assisted interpretation of planar whole-body bone scans.* J Nucl Med, 2008. **49**(12): p. 1958-65.